Title

Predicting Redundancy of a 7 DOF Upper Limb Exoskeleton Toward Improved Transparency between Human and Robot

Journal

Journal of Intelligent & Robotic Systems, 80(Suppl 1)

ISSN

0921-0296

Authors

Kim, Hyunchul
Rosen, Jacob

Publication Date

2015-12-01

DOI

10.1007/s10846-015-0212-4

Peer reviewed

J Intell Robot Syst
DOI 10.1007/s10846-015-0212-4

Predicting Redundancy of a 7 DOF Upper Limb Exoskeleton Toward Improved Transparency between Human and Robot

Hyunchul Kim · Jacob Rosen

Received: 30 April 2014 / Accepted: 26 January 2015

Abstract For a wearable robotic system which includes the same redundancy as the human arm, configuring the joint angles of the robotic arm in accordance with those of the operators arm is one of the crucial control mechanisms to minimize the energy exchange between human and robot. Thus it is important to understand the redundancy resolution mechanism of the human arm such that the inverse kinematics solution of these two coupled systems becomes identical. In this paper, the redundancy resolution of the human arm based on the wrist position and orientation is provided as a closed form solution for the practical robot control algorithm, which enables the robot to form the natural human arm configuration as the operator changes the position and orientation of the end effector. For this, the redundancy of the arm is expressed mathematically by defining the swivel angle. Then the swivel angle is expressed as a superposition of two components, which are reference swivel angle and the swivel angle offset, respectively. The reference swivel angle based on the wrist position is defined by the kinematic criterion that maximizes the manipulability along the vector connecting the wrist and the virtual target point on the head region as a cluster of important sensory organs. Then the wrist orientation change is mapped into a joint angle availablility function output and translated to the swivel angle offset with respect to the reference swivel angle. Based on the inverse kinematic formula the controller can transform the position and orientation of the end-effector into the joint torque which enables the robot to follow up the operator's current joint configuration. The estimation performance was evaluated by utilizing a motion capture system and the results show that there is a high correlation between the estimated and calculated swivel angles.

Keywords Exoskeleton · 7DOF · Redundancy · Swivel angle · Control · Human-robot interface

1 Introduction

Synergy between human arms and wearable robot systems (e.g. the exoskeletons) enables robots to support and assist physical capabilities of the human in various situations. In particular, the advent of high degree of freedom assistive wearable robots [28, 33, 36] enabled more objective and comprehensive rehabilitation programs for people who suffer from a variety of neuromuscular diseases [20, 33, 36, 44]. Healthy humans

H. Kim (✉)
Department of Electrical Engineering, University of California Santa Cruz, 1156 High Street, Santa Cruz, CA 95064, USA
e-mail: hyunchul78@gmail.com

J. Rosen
Department of Mechanical and Aerospace Engineering, University of California Los Angeles, 405 Hilgard Ave, Los Angeles, CA, 90095 USA
e-mail: rosen@seas.ucla.edu

Published online: 18 February 2015

have flexible arm movement to manipulate objects and to avoid obstacles while robotic manipulators can augment power and reduce the fatigue due to heavy loads. By constructively combining the flexibility of natural human movements with the power of manipulation of robots, we can maximally utilize the support from the robot with minimum energy exchange between the wearable robots and their human users. For this, the motor control mechanism, which allows a particular motor task with a large degree of flexibility, needs to be formulated for the practical controller implementation in the assistive robots. In other words, the inverse kinematics solution resolving the redundancy of these two coupled systems must be identical in order to guarantee a seamless integration [18, 36].

Earlier work to reveal the redundancy resolution of the human arm focused on posture-based motion control strategies [6, 7] based on Donders' law, which was originally proposed for eye movements. Most of the early work resolved the redundancy at the kinematic level by focusing on the desired hand posture under the kinematic constraint at a target location. Another line of research focuses on dynamic constraints such as the amount of work and energy [12, 27]. In this context, Soechting and his colleagues [38] proposed that the final arm posture is made by minimizing the amount of work required to move the hand from a starting to an ending position. The minimum-torque-change model is presented in [23, 41]. Tao et al. [12] presented an inverse kinematic solution which defines the natural elbow position by minimizing the total work done by joint torques. For more intuitive and feasible inverse kinematic solution for the human-machine interface, the law for biomimetic trajectory planning of humans was studied and applied to the robot inverse kinematics [1, 34]. For this, dependencies among joint angles are analyzed and modelled by various system identification algorithms such as neural networks, ARX(Auto-Regressive Exogenous) and probabilistic models [10, 21]. Recently in our preliminary work, by focusing on the functional difference between the robotic system and the human, new kinematic constraints which utilize the head as a hidden target position was proposed [14, 18]. In these works, it is shown that natural hand posture for reaching activities is mainly configured to bring the hand efficiently back to the head region. However there are many tasks in daily living which require more sophisticated arm configurations such as rotating the door nob and pouring water into a cup. The redundancy resolution and control scheme mentioned above has limitations in estimating sophisticated human arm movement in various situations as a closed form solution. In order to overcome this limitation, it was tried to directly translate the muscular signal to joint torque information for the robot control based on surface electromyography (sEMG) signal data analysis [3, 39]. In this line of research, the Hill-type muscle model [11] is adopted to predict the muscle force using the EMG signal and its kinematic parameters. Since the human-machine interface based on sEMG signal is established at the neuromuscular level, the control model enables estimating the effects of muscle contractions even before these effects can be visually observed. This provides the basis for modeling more sophisticated control algorithms. However, the sEMG signal based control has fundamental limitations to be adopted as a stable robot control algorithm due to the non-causal EMG signal and the unstable physical contact between the sEMG electrode and the human skin. Thus in this paper, a more comprehensive and robust exoskeleton control algorithm based on the biologically inspired redundancy resolution model is presented. The proposed control model provides the reference swivel angle defined by the wrist position and the kinematic criterion that maximizes the manipulability along the vector connecting the wrist and the virtual target point on the head region as a cluster of important sensory organs. Then the wrist orientation change is mapped into a joint angle availablility function output and translated to the swivel angle offset with respect to the reference swivel angle. Based on the inverse kinematic formula, the controller can transform the position and orientation of the end-effector into the joint torque which enables the robot to follow up the operators's current joint configuration. The estimation performance was evaluated by utilizing a motion capture system and results show that there is a high correlation between the estimated and calculated swivel angles. The proposed work differs from our previous work [13, 17, 18] in the following aspects: 1) the orientation of the wrist is reflected on the swivel angle estimation considering the unique muscular and skeletal structure of the human arm

which makes each arm segment move jointly without relying on the force/torque sensor signal; 2) the swivel angle estimation algorithm is tested on more subjects; 3) the reduced energy exchange based on the proposed control scheme is measured by applying it to the exoskeleton robot. This paper is organized as follows. Section 2 presents the exoskeleton system model and methods describing the forward and inverse kinematics of the robot. Section 3 proposes the swivel angle estimation algorithm based on the wrist position and orientation. Section 4 shows the experimental results to report the proposed swivel angle estimation performance and energy exchange between human and robot. Finally, Section 5 concludes the paper with discussion.

2 System Model and Method

The synchronous movement between the exoskeleton robot and human arm can be guaranteed only when there exists a proper interface between the two. In the following sections, the robotic system and the kinematics of the human arm model supporting natural human arm movements will be introduced.

2.1 Exoskeleton Design Supporting Human Arm Model

The kinematics and dynamics of the human arm during activities of daily living (ADL) were previously studied to determine the design specifications for the upper limb exoskeleton UL-EXO7 [35, 36]. Articulation of the UL-EXO7 is achieved by seven single-axis revolute joints which support 99 % of the range of motion required to perform daily activities [36]. Three revolute joints are responsible for shoulder abduction-adduction, flexion-extension and internal-external rotation. A single rotational joint is employed at the elbow, creating elbow flexion-extension. Finally, the lower arm and hand are connected by a three-axis spherical joint resulting in wrist pronation-supination, flexion-extension, and radial-ulnar deviation. As a human-machine interface (HMI), four six-axis force/torque sensors (ATI Industrial Automation, model-Mini40) are attached to the upper arm, the lower arm, the hand and the tip of the exoskeleton [30]. The force/torque sensor at the tip of the exoskeleton allows measurement of interactions between the exoskeleton and the environment.

2.2 The Extra Degree of Freedom

Since the seven-DOF arm model is redundant, the location and orientation of the hand does not fully specify the configuration of the arm. By also specifying the elbow position, the arm configuration is fully defined. According to the frame definition in Fig. 1a, the elbow position introduces three additional variables where only one additional variable is needed. A single variable can parameterize the elbow. The arm forms a triangle with a point at the shoulder (P_s) one at the elbow (P_e) and the last at the wrist (P_w). Both the shoulder and wrist joints are spherical, and allow rotation of point P_e around the vector ($P_w - P_s$) [Fig. 1b]. A local coordinate system at the center of the elbow circle (P_c), gives a reference to measure the swivel angle (ϕ) of the elbow. A normal vector that points in the direction of ($P_w - P_s$) is defined as:

$$\mathbf{n} = \frac{P_w - P_s}{||P_w - P_s||}. \tag{1}$$

A normalized vector that is projected onto the plane normal to $\mathbf{n}$ is given by:

$$\mathbf{u} = \frac{\mathbf{a} - (\mathbf{a}\cdot\mathbf{n})\mathbf{n}}{||\mathbf{a} - (\mathbf{a}\cdot\mathbf{n})\mathbf{n}||} \tag{2}$$

where $\mathbf{a}$ can be selected as any vector. Badler and Torlani [2] suggest $\mathbf{a}$ to be the $-\mathbf{z}$ vector. This selection has real physical meaning. When ϕ is equal to zero, the elbow is at its lowest possible point. The last vector of the coordinate system ($\mathbf{v}$), is found by taking the cross product of $\mathbf{n}$ and $\mathbf{u}$. Vectors $\mathbf{n}$, $\mathbf{u}$ and $\mathbf{v}$ form an orthonormal coordinate system. Where $\mathbf{u}$ and $\mathbf{v}$ are in the plane of the elbow circle [Fig. 1c]. The radius (R) and center (P_c) of the circle are easily found through geometry:

$$R = U\sin(\Omega) \tag{3}$$

$$P_c = P_s + U\cos(\Omega)\cdot\mathbf{n} \tag{4}$$

$$\cos(\Omega) = \frac{U^2 - L^2 - ||P_w - P_s||^2}{-2L^2||P_w - P_s||}, \tag{5}$$

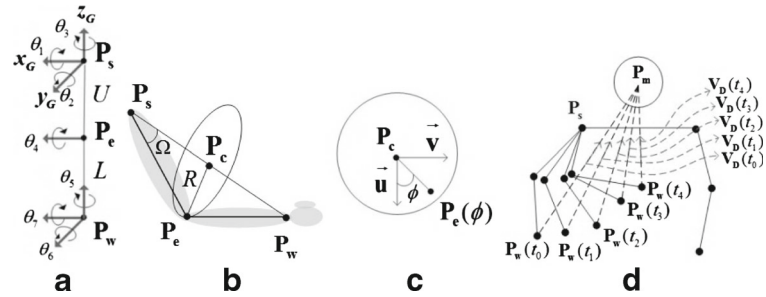

Fig. 1 **a** The global reference frame F_G defined on P_s and joint angles $[\theta_1, \theta_2, \ldots \theta_7]$ for each joint in an initial position of the right arm. **b** The extra degree of freedom is defined by a rotation axis that goes from the shoulder to the wrist. **c** By creating a coordinate frame at the center of the elbow circle, the swivel angle can be defined allowing the parameterizations of the elbow position by a single variable. **d** Virtual destination for the given wrist position at any time t_i. $V_D\,(t_i)$ means the virtual destination formed at any time t_i depending on the wrist position $P_W\,(t_i)$.The pictures were referenced from the original work in [14, 15, 29]

where U and L are the lengths of the upper and lower arm segments [Fig. 1b]. The position of the elbow can now be expressed as a parametrization of ϕ [40]:

$$P_e(\phi) = R\,[\cos(\phi)\mathbf{u} + \sin(\phi)\mathbf{v}] + P_c. \tag{6}$$

Then the inverse kinematics for the 7-DOF exoskeleton robot can be solved by the two following equations:

$$T_1T_2T_3T_4T_5T_6T_7g_{st} = g_d \tag{7}$$

$$T_1T_2P_{e_o} = P_e(\phi), \tag{8}$$

where T_i and g_{st} denote the 4×4 homogeneous transformation matrix defining the rotation and translation with respect to the ith joint axis and the transformation between the tool and the base frames at the initial position of the arm ($\theta = 0$) based on the exponential coordinates system formulation approach [4, 31]. Unlike the Denavit-Hartenberg parameter approach representing the relative motions of each link with respect to the previous link, g_{st} in Eq. 7 translates the end effector P_T in the local tool frame to P_T' in the global base frame. Thus the homogeneous transformation matrix T_i performs the rotations and translations around the ith joint axis represented in the global base frame. There is not a simple one-to-one mapping between the exponential coordinates system and the Denavit-Hartenberg parameters approach [4, 31] but both have the same form of final transformation matrix g_d in Eq. 7. Note that P_{e_o} is the initial position of the elbow and $P_e(\phi)$ is from Eq. 6.

2.3 Inverse Kinematics for the Given Swivel Angle

We will decompose (7) and (8) into one of two subproblems whose solutions are readily available [29].

2.3.1 Subproblem 1

Given the transformation matrix $T(\theta)$, find θ such that:

$$T(\theta)P_0 = P_d. \tag{9}$$

This corresponds to rotating an initial point P_0 about a given axis until it is coincident with P_d, the desired final position. The solution to this problem is:

$$\theta = atan2\left[\boldsymbol{\omega}^T(\mathbf{u} \times \mathbf{v}), \mathbf{u}^T\mathbf{v}\right] \tag{10}$$

$$\mathbf{u} = (P_0 - P_r) - \boldsymbol{\omega}\boldsymbol{\omega}^T(P_0 - P_r) \tag{11}$$

$$\mathbf{v} = (P_d - P_r) - \boldsymbol{\omega}\boldsymbol{\omega}^T(P_d - P_r), \tag{12}$$

where $\boldsymbol{\omega}$ points in the direction of the rotation axis and P_r is a point the axis passes through. For the derivation refer to [4, 31].

2.3.2 Subproblem 2

Given the transformation matrix $T_i(\theta_i)T_j(\theta_j)$ where the rotation axis of T_i and T_j intersect, find θ_i and θ_j such that:

$$T_i(\theta_i)T_j(\theta_j)P_0 = P_d. \tag{13}$$

This corresponds to rotating an initial point P_0 about the rotation axis of T_j by θ_j then about the rotation

axis of T_i by θ_i, so that the final location of the point coincides with P_d the desired final position. The solution to this problem is found by first finding P_g as follows:

$$P_g = \alpha\boldsymbol{\omega}_i + \beta\boldsymbol{\omega}_j \pm \sqrt{\gamma}(\boldsymbol{\omega}_i \times \boldsymbol{\omega}_j) + P_r \tag{14}$$

$$\alpha = \frac{\left(\boldsymbol{\omega}_i^T\boldsymbol{\omega}_j\right)\boldsymbol{\omega}_j^T(P_0 - P_r) - \boldsymbol{\omega}_i^T(P_d - P_r)}{\left(\boldsymbol{\omega}_i^T\boldsymbol{\omega}_j\right)^2 - 1} \tag{15}$$

$$\beta = \frac{\left(\boldsymbol{\omega}_i^T\boldsymbol{\omega}_j\right)\boldsymbol{\omega}_i^T(P_d - P_r) - \boldsymbol{\omega}_j^T(P_0 - P_r)}{\left(\boldsymbol{\omega}_i^T\boldsymbol{\omega}_j\right)^2 - 1} \tag{16}$$

$$\gamma = \frac{||(P_0 - P_r)||^2 - \alpha^2 - \beta^2 - 2\alpha\beta\boldsymbol{\omega}_i^T\boldsymbol{\omega}_j}{||\boldsymbol{\omega}_i \times \boldsymbol{\omega}_j||^2}, \tag{17}$$

where $\boldsymbol{\omega}_i$ and $\boldsymbol{\omega}_j$ point in the direction of the rotation axes of T_i and T_j and P_r is the point where the axes intersect. There may be zero, one or two real solutions for P_g depending on γ. If solutions exist, then θ_i and θ_j can be found with subproblem one:

$$T_i(-\theta_i)P_d = P_g \tag{18}$$

$$T_j(\theta_j)P_0 = P_g. \tag{19}$$

For the derivation of this solution refer to [31, 42].

2.3.3 Decomposition of the Forward Kinematics

θ_4 can easily be solved by an application of the law of cosine:

$$\theta_4 = \pi - \frac{L^2 + U^2 - ||w - s||^2}{2LU}. \tag{20}$$

Equation 8 is already in the form of Eq. 13 with $P_0 = P_{e_0}$ and $P_d = P_e(\phi)$, and an immediate solution for θ_1 and θ_2 is available. Note that Eq. 13 has two solutions. For a natural arm configuration the negative sign in Eq. 14 should be chosen.

Next to solve for θ_3, Eq. 7 is premultiplied by $(T_1T_2)^{-1}$ and then postmultiplied by $g_{st}^{-1}P_{w_0}$. Since P_{w_0} is an eigenvector of T_5, T_6 and T_7 with eigenvalue one, $T_5T_6T_7P_{w_0} = P_{w_0}$. Then we have

$$T_3\left(T_4P_{w_o}\right) = (T_1T_2)^{-1}g_d g_{st}^{-1}P_{w_0}. \tag{21}$$

This is in the form of Eq. 9 when $P_0 = (T_4P_{w_0})$ and $P_d = (T_1T_2)^{-1}g_d g_{st}^{-1}P_{w_0}$.

To solve for θ_5 and θ_6, Eq. 7 is premultiplied by $(T_1T_2T_3T_4)^{-1}$ and postmultiplied by $g_{st}^{-1}P_7$, where $P_7 = [1, 0, -U - L]^T$ which is an eigenvector of T_7 with an eigenvalue of one. Then we have $T_7P_7 = P_7$ and

$$T_5T_6P_7 = (T_1T_2T_3T_4)^{-1}g_d g_{st}^{-1}P_7. \tag{22}$$

This is now in the form of Eq. 13 when $P_0 = P_7$ and $P_d = (T_1T_2T_3T_4)^{-1}g_d g_{st}^{-1}P_7$. Equation 13 has multiple solutions and the negative sign in Eq. 14 should be chosen.

Finally to solve for θ_7, Eq. 7 is Premultiplied by $(T_1T_2T_3T_4T_5T_6)^{-1}P_s$ and then postmultiplied by $g_{st}^{-1}P_s$ as follows:

$$T_7P_s = (T_1T_2T_3T_4T_5T_6)^{-1}g_d g_{st}^{-1}P_s. \tag{23}$$

Equation 23 is in the form of Eq. 9. Note that $P_0 = P_s$ and $P_d = (T_1T_2T_3T_4T_5T_6)^{-1}g_d g_{st}^{-1}P_s$ in Eq. 9.

3 Swivel Angle Estimation

Considering the high complexity of the human brain network, it is hard to define the general redundancy resolution (swivel angle estimation) mechanism of the human arm and to apply this to the robot as a real time control mechanism. However in our previous work [18], it was studied that the human arm swivel angle could be effectively estimated by a simple closed form equation in a kinematic level when the given tasks did not require wrist orientation changes and fast hand movement without load. The estimation performance became worse when there was an excessive wrist orientation variation during the experiment. Thus assuming that the hand movement speed is not fast in an activity of daily life, we can infer that the generalized swivel angle estimation model could be established by compensating the deviated swivel angle caused by the excessive wrist orientation changes. To make the estimation problem more practical for real time application, it is hypothesized that the swivel angle components from the wrist orientation and position are mutually independent such that the final form of swivel angle estimation can be represented as follows:

$$\phi_{fin} = \phi_{ref}(\theta_1, \theta_2, \theta_3, \theta_4) + \Delta\phi(\theta_5, \theta_6, \theta_7), \tag{24}$$

where ϕ_{ref} and $\Delta\phi$ are based on the wrist position and orientation respectively. The entire control scheme based on Eq. 24 is also depicted in Fig. 2. This linear

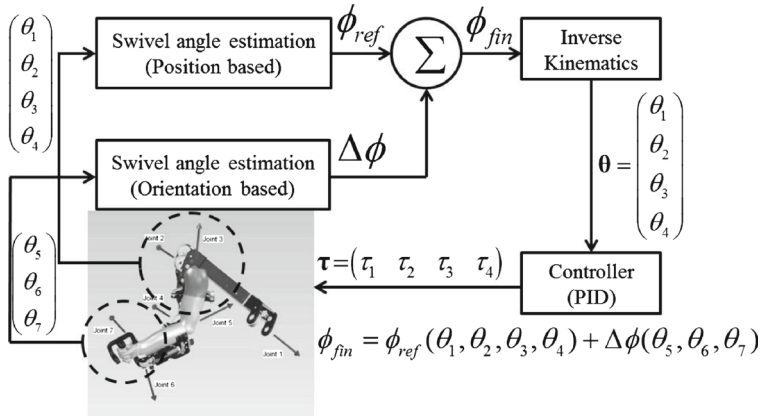

Fig. 2 Block diagram of the control scheme: The final swivel angle ϕ_{fin} is a combination of position based swivel angle ϕ_{ref} and orientation based swivel angle $\delta\phi$. ϕ_{fin} will be converted to the joint torque to configure the desired swivel angle on the exoskeleton. The original figure can be found in [18]

combination model can be replaced with more sophisticated non-linear system model or include the cross term between wrist position and orientation as a future work. Also note that throughout the paper the swivel angle estimation is limited to the tasks that do not require fast hand movement and load such that the dynamics of the human arm could be neglected.

3.1 Swivel Angle Based on the Wrist Position

Given the role of the head as a cluster of sensing organs and the importance of arm manipulation to deliver food to the mouth, it is hypothesized that the prime goal of the arm manipulation is to efficiently retract the palm to the head region such that the swivel angle for the natural and unconstrained arm movement is chosen to meet the prime goal of the human arm manipulation by the motor control system. This hypothesis is supported by the intracortical stimulation experiments to evoke coordinated forelimb movements in the awake primate [5, 8]. It has been reported that each stimulation site produced a stereotyped posture in which the arm moved to the same final position regardless of its posture at the initial stimulation. In the most complex example, the monkey formed a frozen pose with the hand in a grasping position in front of the open mouth. This implies that during the arm movement toward an actual target, the virtual target point on the head can be set for the potential retraction position of the palm as shown in Fig. 1d and the movement toward that virtual target point should be efficient. The proposed prime goal can be utilized as an additional constraint reflecting the biological aspect of the human arm movement and will play a major role in reanimating the human arm movement more naturally than the other purely engineering constraints such as minimum energy and torque.

3.1.1 Manipulability Ellipsoid

To extract the equation that resolves the redundancy of the human arm from the notion of efficient arm movement toward the head, the concept of manipulability ellipsoid is adopted. Let P_m denote the virtual target position at the center of the head in Fig. 3a. When we consider the combinations of joint velocities satisfying the condition in which $\Sigma_{i=1}^{n}\dot{\theta}_i^{\,2} = 1$, the hand velocity as a function of the joint velocity is described by an ellipsoid that defines the arm's scaled Jacobian. The largest among the major axes of the manipulability ellipsoid defines the direction of the highest sensitivity and efficiency where the end effector velocity varies in response to the joint space velocity [Fig. 3b] [26]. The property of the manipulability ellipsoid is described in Lemma 1.

Lemma 1 *Let the plan S be defined by three points P_w, P_e and P_s. The longest axis of the manipulability ellipsoid is aligned along plane S and its magnitude σ_1 is expressed as*

$$\sigma_1 = \sqrt{\lambda_1} = \sqrt{\left(\left(L_{ws}^2 + L_{we}^2\right) + \left(L_{ws}^2 + L_{we}^2\right)c_1\right)/2} \qquad (25)$$
$$c_1 = \sqrt{1 - c_2},\ c_2 = 4L_{we}^2 L_{ws}^2 \sin(\varphi)^2 / \left(L_{ws}^2 + L_{we}^2\right)^2.$$

The proof can be found in [17] and the Appendix.

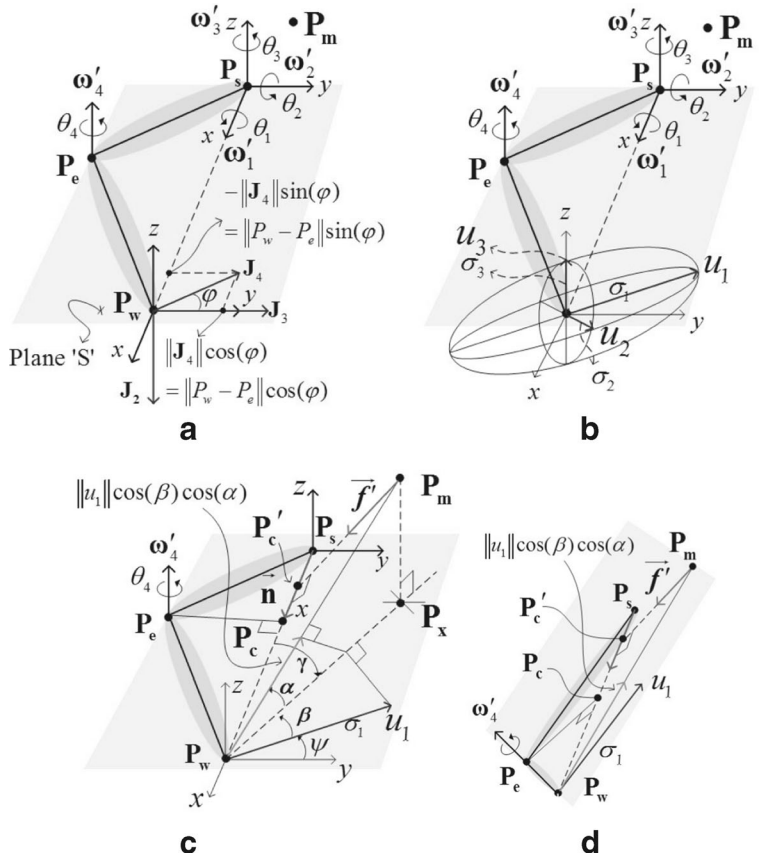

Fig. 3 The new coordinate system composed of P_w, P_e, P_s and P_m. **a** Each element J_i in the Jacobian matrix is defined with respect to the newly defined frame on the shoulder where the x axis is defined as $(P_w - P_s)/\|P_w - P_s\|$ and the y axis sits on the plane S composed of P_w, P_e and P_s. The new frame on the shoulder is defined for the convenience of the calculation. **b** Manipulability ellipsoid on the wrist position. u_1, u_1 and u_3 indicate the three major axes of the ellipsoid with magnitude of σ_1, σ_2 and σ_3. **c** The highest manipulability direction vector u_1 projected on the $(P_m - P_w)/\|P_m - P_w\|$ is marked as the green arrow and its magnitude can be represented as $\|u_1\|\cos(\alpha)\cos(\beta)$. **d** This figure shows the specific elbow position for the given wrist position that maximizes the manipulability projected on the virtual trajectory. When P_m, P_s, P_e and P_w are on the same plane, the manipulability on the virtual trajectory is maximized. The pictures were referenced from the original work in [14, 15, 29]

3.1.2 Optimum Swivel Angle

Assuming that the virtual hand movement follows the shortest path connecting P_w to P_m, the swivel angle for the efficient hand movement is chosen such that the projection of the major axis u_1 of the manipulability ellipsoid onto $(P_m - P_w)$ will be maximized [Fig. 3c]. Then the optimum swivel angle can be found by establishing (26). Since we have already shown the detailed description of the optimum swivel angle estimation algorithm in [18], here we only explain the basic idea and the result. Let:

$$\phi = \underset{\alpha,\beta\in[0\ \pi/2]}{\arg\max} \left[u_1^T\ (P_m - P_w)\right] \tag{26}$$

$$= \underset{\alpha,\beta\in[0\ \pi/2]}{\arg\max}\ [\|u_1\|\|P_m - P_w\|\cos(\alpha)\cos(\beta)], \tag{27}$$

where α and β are the angles between $(P_m - P_w)$ and plane S, and the angle between u_1 and the projection of $(P_m - P_w)$ onto S [Fig. 3c] respectively. Note that

the projected portion of u_1 onto $(P_m - P_w)$ is represented by $\|u_1\| \cos(\alpha) \cos(\beta)$ and marked as an arrow in Fig. 3c. Based on the geometry defined in Fig. 3c, Eq. 44 is maximized when $\alpha = 0$ regardless of the β determined by the given wrist position. In this condition when $\alpha = 0$, plane S is coplanar with the plane composed by P_m, P_s and P_w as shown in Fig. 3d. Then the swivel angle under this condition is calculated given the known positions P_m, P_w and P_s. In order to do so, a new vector $\mathbf{f} = P_w - P_m$ is defined. The vector $\mathbf{f}'$ is the projection of $\mathbf{f}$ on the direction of $P_w - P_c'$ in Fig. 3c. Based on the fact that $\mathbf{f}'$ is parallel to vector $P_e(\phi) - P_c$ when $\alpha = 0$, the swivel angle is estimated by

$$\phi_{ref} = \arctan 2 \left(\mathbf{n} \cdot \left(\mathbf{f}' \times \mathbf{u} \right), \mathbf{f}' \cdot \mathbf{u} \right). \tag{28}$$

The estimation algorithm is proper for the real time inverse kinematic solution due to its simplicity. The accuracy of the ϕ_{est} estimation was assessed based on the experimental protocol described in the Section 4.

3.2 Swivel Angle Based on the Wrist orientation

Unlike conventional robots, the human arm has a unique muscular and skeletal structure which makes each arm segment move jointly. For instance, when the wrist rotates to pour the water into the cup, one or more of the wrist joints in the seven DOF arm model [Fig. 1a] can approach the joint limit due to the limited range of the motion and one unconsciously starts to use other joints such that all the joints in the human arm do not reach their joint limit. Human motor control tends to choose the joint configuration which avoids the joint limit of each joint. To quantify how much all joints approach the joint limit in aggregate, the joint angle availability function [24, 25, 32] can be considered as follows:

$$C = \sum_{i=1}^{n} w_i \left(\frac{\theta_i - \theta_{i_{ref}}}{\Delta\theta_i} \right)^2, \tag{29}$$

where $\Delta\theta_i = (\max\theta_i - \min\theta_i)/2$ is the range of each joint, $\theta_{i_{ref}} = (\max\theta_i + \min\theta_i)/2$ is the neutral position of each joint and w_i is the weighting coefficient that reflects the effect on C. This function has the following property. When θ_i approaches the joint limits which are $\max\theta_i$ or $\min\theta_i$ in Eq. 29, C becomes $\sum_{i=1}^{n} w_i$. When θ_i approaches the θ_{ref} in Eq. 29, C becomes zero. Thus C ranges over $\left[0 \ \sum_{i=1}^{n} w_i\right]$. In order to relate the wrist orientation to the swivel angle, we can focus on the joint availability function output on the wrist in Eq. 30, modified from Eq. 29, and relate this to the swivel angle change.

$$C = w_1 \left(\frac{\theta_5 - \theta_{5_{ref}}}{\Delta\theta_5} \right)^2 + w_2 \left(\frac{\theta_6 - \theta_{6_{ref}}}{\Delta\theta_6} \right)^2 + w_3 \left(\frac{\theta_7 - \theta_{7_{ref}}}{\Delta\theta_7} \right)^2. \tag{30}$$

3.2.1 Joint Angle Availability Function and Swivel Angle

The modified joint angle availability function in Eq. 30 quantitatively defines how much the wrist joints approach the joint limit in aggregate. Then it is possible to map this specific function output to the corresponding swivel angle as a function of wrist orientation. For this, the following three conditions were considered for the algorithm implementation between the modified joint angle availability function output and the swivel angle.

1. Once the availability function output reaches the maximum $\sum_{i=1}^{n} w_i$ or minimum value 0, the deviated swivel angle $\Delta\phi$ in Eq. 24 is saturated to its maximum or minimum value.
2. The proper weighting coefficient w_i for each wrist joint should be estimated considering the different effect of each wrist joint on the swivel angle.
3. Asymmetric muscular structure of the human arm having different muscular tension needs to be considered: we defined two regions where $\phi_{fin} \leq \phi_{ref}$ and $\phi_{fin} > \phi_{ref}$. In each region, it is assumed that there is a different mapping between swivel angle $\Delta\phi$ and the joint availability function as shown in Fig 5.

The simplest form of relation will be the linear mapping of the ergodic function as shown in Fig. 4a. The alternative choice can be a non linear sigmoid function as shown in Fig. 4c. Since the sigmoid function has an advantage against the linear mapping which comes from the fact that the output of the sigmoid function approaches an asymptotic bound in a closed form and there is no abrupt transition in the function output, we adopted a sigmoid function in our application. The basic form of sigmoid function in Fig. 4b is modified to map the joint availability

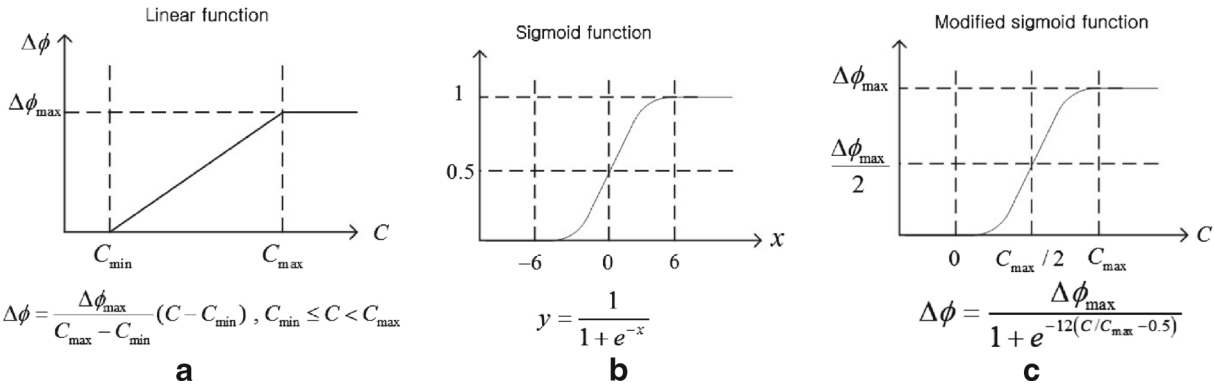

Fig. 4 Mapping between the ergodic function and the swivel angle (**a**) linear mapping between the ergodic function and the swivel angle and (**b**) basic form of sigmoid function (**c**) non-linear mapping based on sigmoid function between the joint availability function and swivel angle change. The modified sigmoid function was scaled and shifted from the basic form of sigmoid function in (**b**)

function output to the corresponding swivel angle as shown in Fig. 4c.

$$\Delta\phi = \frac{\Delta\phi_{max}}{1+\exp\left(-12\left(\frac{C}{C_{max}}-0.5\right)\right)} \tag{31}$$

$$\Delta\phi_{max} = \begin{cases} \phi_{ref} - \min(\phi_{fin}) & , \phi_{fin} \le \phi_{ref} \\ \max(\phi_{fin}) - \phi_{ref} = -\phi_{ref} & , \phi_{fin} > \phi_{ref} \end{cases},$$

where $\phi_{ref} \le 0$ and $\min(\phi_{fin}) \le 0$ based on our swivel angle definition in Fig. 1. Note that the $\max(\phi_{fin}) = 0$ when the elbow is at its lowest position. Then Eq. 30 can be combined with Eq. 31 for $\phi_{fin} \le \phi_{ref}$ and $\phi_{fin} > \phi_{ref}$ respectively as follows:

$$\begin{aligned} \frac{C}{C_{max}} &= -\frac{1}{12}\log\left(\frac{\Delta\phi_{max}}{\Delta\phi}-1\right)+0.5 \\ &= \frac{w_1}{C_{max}}\left(\frac{\theta_5-\theta_{5_{ref}}}{\Delta\theta_5}\right)^2 \end{aligned} \tag{32}$$

$$\begin{aligned} &+\frac{w_2}{C_{max}}\left(\frac{\theta_6-\theta_{6_{ref}}}{\Delta\theta_6}\right)^2 \\ &+\frac{w_3}{C_{max}}\left(\frac{\theta_7-\theta_{7_{ref}}}{\Delta\theta_7}\right)^2 \\ \Longrightarrow C' &= w_1'\theta_5' + w_2'\theta_6' + w_3'\theta_7', \end{aligned} \tag{33}$$

where $C' = \frac{C}{C_{max}}$, $w_i' = \frac{w_i}{C_{max}}$ and $\theta_i' = \left(\frac{\theta_7-\theta_{7_{ref}}}{\Delta\theta_7}\right)^2$. Note that Eq. 32 can be achieved by rearranging Eq. 31 and applying the log on both sides of the equation. To estimate w_i in Eq. 33, joint angle data can be collected by the motion capture system for the specific tasks that require wrist orientation changes. By using the joint angle information, Eq. 33 can be extended as

$$\begin{aligned} C'(t_0) &= w_1'\theta_5'(t_0) + w_2'\theta_6'(t_0) + w_3'\theta_7'(t_0) \\ C'(t_1) &= w_1'\theta_5'(t_1) + w_2'\theta_6'(t_1) + w_3'\theta_7'(t_1) \\ &\vdots \\ C'(t_{N-1}) &= w_1'\theta_5'(t_{N-1}) + w_2'\theta_6'(t_{N-1}) + w_3'\theta_7'(t_{N-1}). \end{aligned} \tag{34}$$

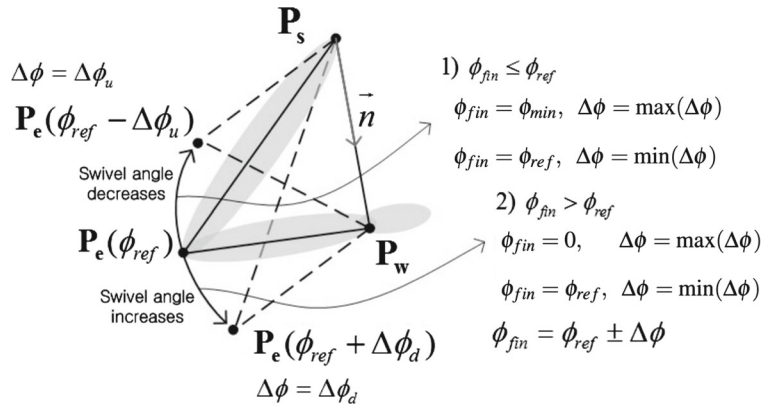

Fig. 5 Deviated swivel angle $\Delta\phi(\Delta\phi_u, \Delta\phi_d)$ from ϕ_{ref} in two swivel angle ranges: $\phi_{fin} \le \phi_{ref}$ and $\phi_{fin} > \phi_{ref}$

Then the matrix representation of Eq. 34 is given by

$$\mathbf{C} = \mathbf{E} \cdot \mathbf{W} \tag{35}$$

$$\mathbf{C} = [C'(t_0)C'(t_1)\ldots C'(t_{N-1})]^T, \quad \mathbf{W} = \left[w_1' w_2' w_3'\right]^T$$

$$\mathbf{E} = \begin{pmatrix} \theta_5'(t_0) & \theta_6'(t_0) & \theta_7'(t_0) \\ \theta_5'(t_1) & \theta_6'(t_1) & \theta_7'(t_1) \\ & \vdots & \\ \theta_5'(t_{N-1}) & \theta_6'(t_{N-1}) & \theta_7'(t_{N-1}) \end{pmatrix}.$$

Since $\sum_i w_i^2$ should be bounded by some constant, an additional constraint is necessary in Eq. 35. Without loss of generality $\sum_i w_i^2 = 1$ can be applied to Eq. 35 as a regulation factor. Then Eq. 35 is reformulated as:

$$\begin{aligned} &\mathbf{C} = \mathbf{E} \cdot \mathbf{W} \\ \rightarrow\ &\widehat{\mathbf{W}} = \min\left[\|\mathbf{C} - \mathbf{E} \cdot \mathbf{W}\|^2 + \lambda \|w\|^2\right]. \end{aligned} \tag{36}$$

The solution to Eq. 36 is well known in literature [9, 43] and the closed form solution is given by

$$\widehat{\mathbf{W}} = \left(\mathbf{E}^T\mathbf{E} + \lambda \cdot \mathbf{I}\right)^{-1} \mathbf{E}^T \cdot \mathbf{C}, \tag{37}$$

where λ is iteratively found to make $\|\mathbf{W}\|^2 = 1$ based on the Matlab simulation. Then the swivel angle estimation model as a function of wrist orientation is fully defined.

Once all the joint angles are collected from a specific subject, $\mathbf{C}$ and $\mathbf{E}$ in Eq. 32 as a function of swivel angle and joint angles can be constructed to estimate $\mathbf{W}$ based on Eq. 37. Once $\mathbf{W}$ is estimated, it can be imported to the robot controller to compute $\frac{C}{C_{max}}$ based on Eq. 35. Then by plugging $\frac{C}{C_{max}}$ into Eq. 31, $\Delta\phi$ can be achieved. Note that as mentioned above, the whole estimation process was individually defined for two cases where $\phi_{fin} \leq \phi_{ref}$ and $\phi_{fin} > \phi_{ref}$ for more precise estimation results.

4 Experiments

The proposed swivel angle estimation model requires parameter estimation respectively for ϕ_{ref} and $\Delta\phi$. In order to verify the proposed swivel angle estimation model, the kinematic data of the human arm was collected using the Phasespace motion capture system (Phasespace, Inc.) including eight cameras with sub-millimeter accuracy. Active LED makers were attached to a subject's body at key anatomical locations including shoulder(P_s), elbow(P_e), wrist(P_w) and chest(P_{ch})[Figs. 6a and b]. The markers' locations were sampled at 240 Hz.

Since ϕ_{ref} is defined by the wrist position, the experimental setup for ϕ_{ref} does not include the wrist orientation changes. On the other hand for $\Delta\phi$ estimation, wrist positions were fixed at the specific position and subjects were requested to only change the wrist orientation to minimize the wrist position effect. In the following section, we first conducted two experiments to estimate ϕ_{ref} and $\Delta\phi$. Then the application of the proposed swivel angle estimation to the EXO-UL7 and energy exchange analysis will be introduced. The result shows that the averaged absolute error between measured and estimated swivel angle is on average 3.98 and 3.77 degree for ϕ_{ref} and $\Delta\phi$ respectively. In addition the exoskeleton with proposed swivel angle estimation can reduce the energy exchange by up to 34 %.

4.1 Experiments for Swivel Angle Based on the Wrist Position

In order to define ϕ_{ref} for the unconstrained reaching tasks, three types of reaching tasks were derived from activities of daily living as shown in Figs. 7a and b.

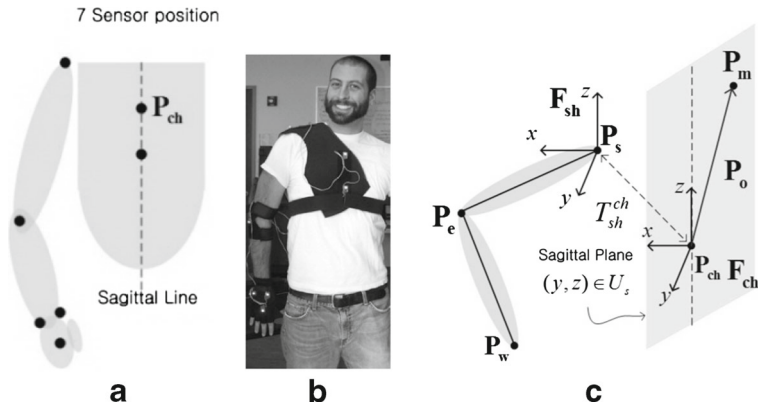

Fig. 6 Experimental setup: **a** and **b** show the LED marker position to collect the kinematic data based on the motion capture system. **c** Frames attached to the chest LED marker position. The original figure can be found in [14]

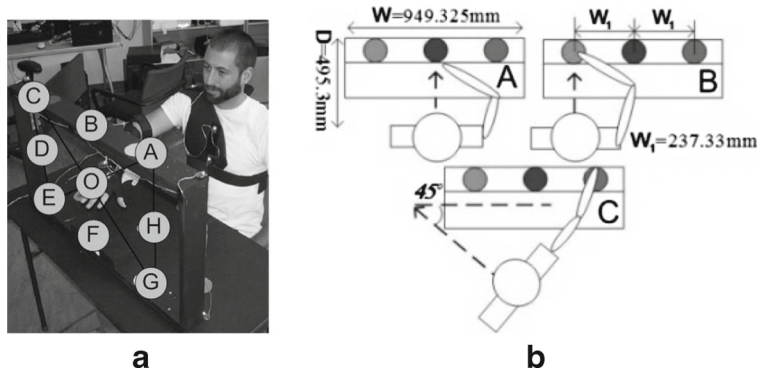

Fig. 7 Experimental setup: **a** Target locations and dimensions of the experimental set up: distance from the table-top to the top-of-shelf = 501.65 mm; height of the table-top from the ground = 736.6 mm. **b** Three types of reaching tasks. In type 'A' and 'B', torso is facing the center and left target respectively while in type 'C' the torso is turned 45 degrees counterclockwise off the Sagittal alignment and hand points to the rightmost target in the abducted posture. The original figure can be found in [13]

Ten right handed healthy subjects participated in the experimental protocol. Of the ten subjects, seven were males and three were females. The age of the subjects ranges from 20 to 40. Each subject was tested in three different sitting postures with his/her torso restrained from torsional movements. The distance between the subject and the table was adjusted based on the length of the subject's arm in order to a avoid a full stretch of the arm (singular configuration). In body posture A (Fig. 7b), the subject faced the table and his/her body was positioned such that the table and the subject's body center lines were aligned. In body posture B, the subject faced the table as previously, but the center line was shifted to the left such that it was aligned with the edge of the table. In body posture C, the body of the subject alignment was the same as in (B) but the torso was rotated by 45 degrees counterclockwise.

4.1.1 Targets and Objects

In this experiment, subjects used his/her index finger to point to the designated targets. Each subject was instructed to position the hand in an initial location ('o') and then move the hand in a self paced fashion between predefined locations as defined in the following order for five cycles [Fig. 7b].

$o \rightarrow a \rightarrow b \rightarrow c \rightarrow d \rightarrow e \rightarrow f \rightarrow g \rightarrow h$(one cycle).

4.1.2 Optimum P_m Estimation

Given the anthropometric differences between the subjects the optimal target location P_m for each subject was calculated. The human body is considered to be symmetric and torsional movement of the torso is ignored. The LED markers P_{ch} on the chest as well as P_m are therefore located on the Sagittal plane [Fig. 6]. A reference frame F_{ch} is attached to P_{ch}. As a result, the location of P_m is represented by a fixed vector (time invariant) P_o expressed in frame F_{ch} (the Sagittal plane) as follows:

$$\begin{bmatrix} P_m(t) \\ 1 \end{bmatrix} = \begin{bmatrix} P_{ch}(t) \\ 1 \end{bmatrix} + T_{sh}^{ch}(t) \begin{bmatrix} P_o \\ 1 \end{bmatrix}, \tag{38}$$

where P_o is a vector representing a constant time-invariant translation offset from P_{ch} expressed in frame P_{ch} and T_{sh}^{ch} is the homogeneous transform matrix between the frame attached to the shoulder and the frame attached to the chest as depicted in Fig. 6c. Then according to Eq. 28, the optimum offset P_o is chosen to minimize the difference between $\phi(t)_{est}$, estimated swivel angle based on Eq. 28, and $\phi(t)_{act}$, calculated swivel angle given the measured joint angels:

$$\arg\min_{y,z \in U_s} \int_y \int_z \left(\int_{t_x}^{t_x+T} |\phi(t)_{act} - \phi(t, P_o(y,z))_{est}| dt \right) dz dy, \tag{39}$$

where U_s represents (y, z) coordinate pairs on the Sagittal plane [Fig. 6c]. Since it is assumed that P_m is located on the Sagittal plane, x_{opt} is the same as the x coordinate of $P_{ch}(t)$. Only a subset of the data were used to calculate the optimal location of P_m, as a result, T in Eq. 39 corresponds to 1/5 of total data recording time. The estimated location of

Table 1 Average absolute differences between measured and estimated swivel angles for the experiment in Sections 4.1 and 4.2

Subj	$\phi_{ref}(^\circ)$			$\Delta\phi(^\circ)$						$P_o(y,z)$
	A	B	C	P_{m1}	P_{m2}	P_{m3}	P_{d1}	P_{d2}	P_{d3}	(cm)
1	2.3±1.5	2.7±1.9	3.8±3.0	5.1±8.0	7.1±7.0	2.9±5.8	2.1±8.6	9.2±8.2	6.2±9.0	(-16,28)
2	3.2±2.3	4.0±2.6	2.1±1.4	1.3±7.3	4.5±8.3	6.5±7.0	4.0±5.2	5.0±4.7	6.4±9.5	(-14,32)
3	5.4±2.7	6.3±3.0	7.1±3.4	2.1±5.4	3.1±1.09	1.6±8.4	1.8±4.4	4.0±3.8	6.2±8.0	(-16,39)
4	5.1±2.6	3.8±2.2	3.1±1.7	3.7±7.3	4.6±7.9	3.9±7.5	1.1±7.6	3.7±7.6	6.0±9.3	(-7,29)
5	8.1±4.3	4.6±2.8	3.4±2.1	3.0±3.3	2.8±9.9	2.9±1.2	1.5±8.9	2.5±5.4	2.9±8.1	(-16,17)
6	4.2±1.3	4.3±2.5	2.4±3.1	4.5±4.0	4.5±5.0	4.2±8.8	1.2±2.5	3.0±2.1	4.5±9.1	(-16,28)
7	5.2±2.3	2.9±2.1	2.2±1.2	3.3±5.5	2.3±4.1	5.5±6.0	2.3±7.3	2.2±4.1	5.1±6.5	(-14,132)
8	6.2±4.4	4.4±3.0	3.2±3.2	5.3±4.4	5.4±3.3	3.0±8.4	4.1±2.6	3.3±3.0	5.7±4.9	(-16,39)
9	4.1±2.2	3.8±3.5	3.0±2.6	2.6±4.4	3.3±5.4	3.1±7.5	3.7±4.2	1.8±2.1	4.4±5.5	(-7,29)
10	3.7±3.1	3.0±2.1	1.9±2.4	3.3±2.3	2.1±4.2	2.0±1.1	2.8±5.4	6.6±4.0	3.8±7.9	(-16,17)

(y, z) defining P_o is summarized in the last column of Table 1.

The computed swivel angle (ϕ_{act}) based on the collected kinematic data was compared with swivel angle ϕ_{ref} estimated by Eq. 28. Figure 8 shows the direct comparison and the average estimation error for the given wrist position is summarized in Table 1.

4.2 Experiments for Swivel Angle Based on the Wrist Orientation

In order to define the effect of wrist orientation on $\Delta\phi$, subjects were requested to reach specific target positions in Fig. 9 and then change the orientation of the wrist. To precisely locate the subject's hand on the desired position and help subjects finding the target location in space, a 6-DOF industrial robot (DENSO) was programmed to project laser on the target location as shown in Fig. 9. Thus subjects visually know where to put their wrist in space by looking at the laser mark projected on their wrist. In this setup subjects were requested to pose in two different body postures and in each posture they were requested to place their arm in three different target locations. Considering the most frequent activities of daily life such as rotating a door nob and pouring water, the subjects were asked to rotate their wrists inward and outward five times as if they would rotate a door nob. Using this data, Eq. 37 will be solved to estimate $\mathbf{W}$.

Note that the proposed experimental setup is simplified for the practical reason considering the fact that most of the tasks which require wrist orientation occur within 45 degree between body and arm [Fig. 9b]. To reveal a more general relationship between the wrist orientation and the swivel angle, more sophisticated experiments should be designed to estimate $\mathbf{W}$.

Similarly from ϕ_{ref}, the computed swivel angle change ($\phi_{act} - \phi_{ref}$) based on the collected kinematic data was compared with the estimated swivel angle change $\Delta\phi$ estimated by Eq. 31. Figure 11 shows the direct comparison result and the estimation error at six different target points is summarized in Table 1. In addition, the statistical analysis for the weighting coefficients $\mathbf{W}$ were plotted as a box plot to see the relative effect of each wrist joint on the swivel angle for the given tasks in Fig. 12.

4.3 Application of Proposed Swivel Angle Estimation to UL-EXO7

In order to verify the performance of the proposed redundancy resolution mechanism, we applied the proposed swivel angle estimation algorithm to the UL-EXO7 controller and designed simple computer game interface that can interact with the robot. The encoder and F/T (Force/Torque) sensor readouts from the UL-EXO7 are transmitted to the game PC through UDP protocol based on the Matlab XPC/Host Target Interface. There are three (6 axis) F/T sensors in each robot arm and they are located at the upper arm, lower arm and the hand [30]. Thus subjects who wear exoskeleton can see their arm moving in the display as shown in Fig. 10. There are four different target configurations in the given game and subjects are instructed to

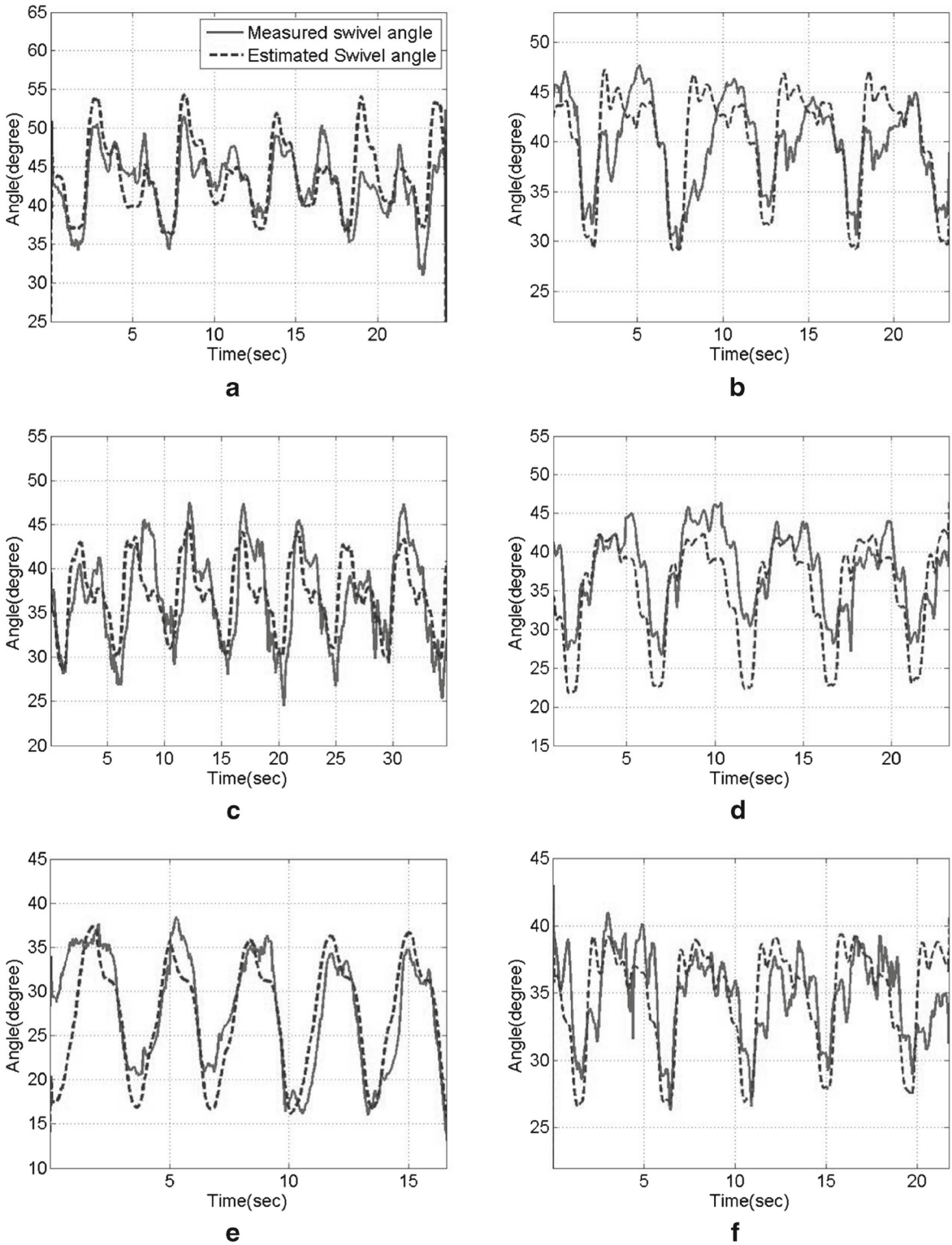

Fig. 8 Comparison between estimated swivel angle (dotted line) and calculated swivel angle (solid line) from two different subjects for Type one task. Each row of the figure shows the comparison result for Type one (A), Type one (B) and Type one (C) from the subjects. Figures **a**, **c**, and **e** are for subject 1 while figures **b**, **d**, and **f** are results from subject 2

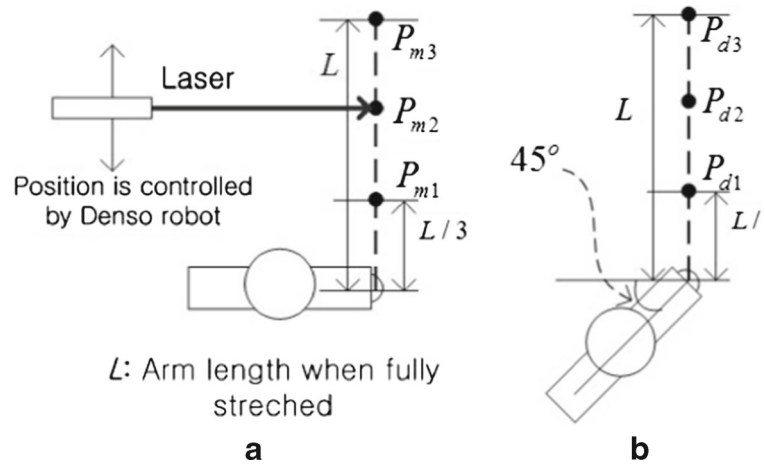

Fig. 9 Experimental setup to estimate **W**. Subjects are requested to face the front in two different postures where the torso is not rotated (**a**) and rotated by 45 degree (**b**). For each torsional configuration, they place the hands in three different locations. For this, we used six axis Denso robot that has a laser pointer at the tool frame. Denso places the laser pointer in parallel with the target point and projects laser to one of the target location (P_{m1}, P_{m2}, P_{m3}, P_{d1}, P_{d2}, P_{d3})

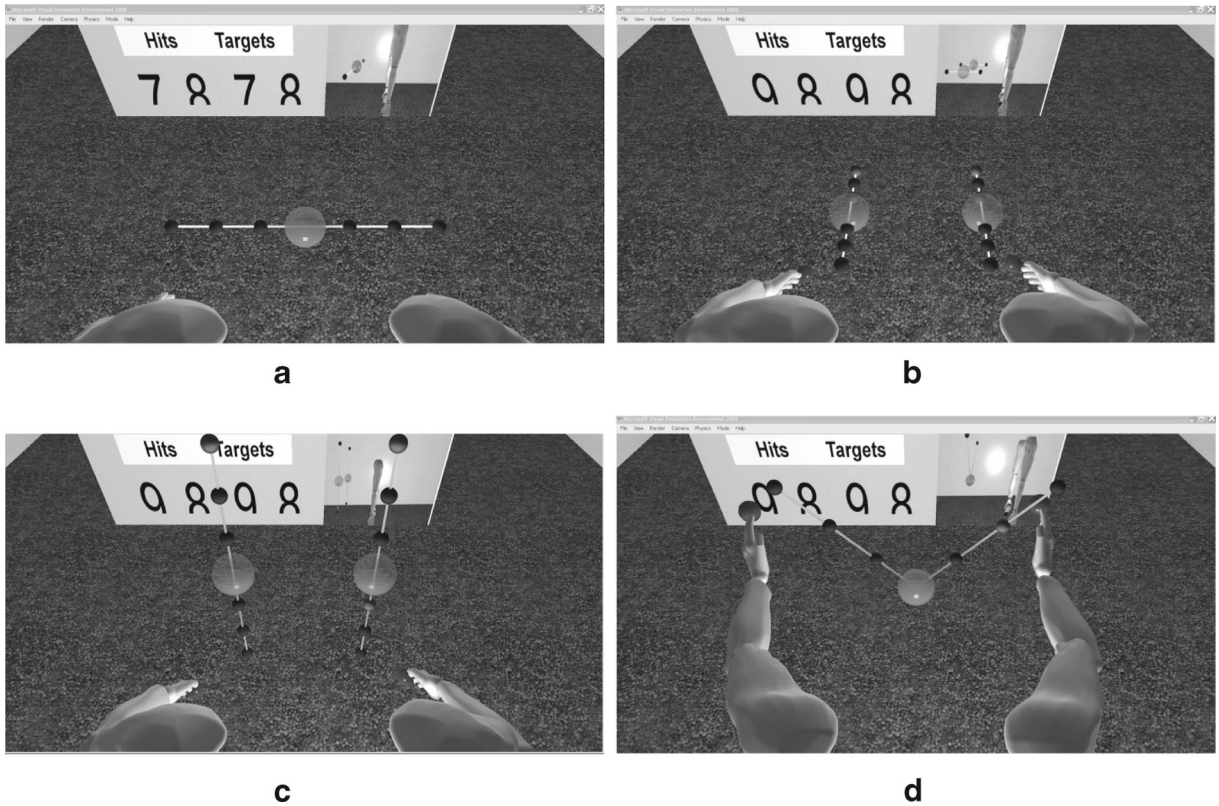

Fig. 10 Virtual reality game for performance estimation. **a** Set 1: targets on the horizontal line, **b** Set 2: targets on the horizontal line rotated by 90 degrees, **c** Set 3: targets on the vertical lines and **d** Set 4: targets on V shaped lines targets

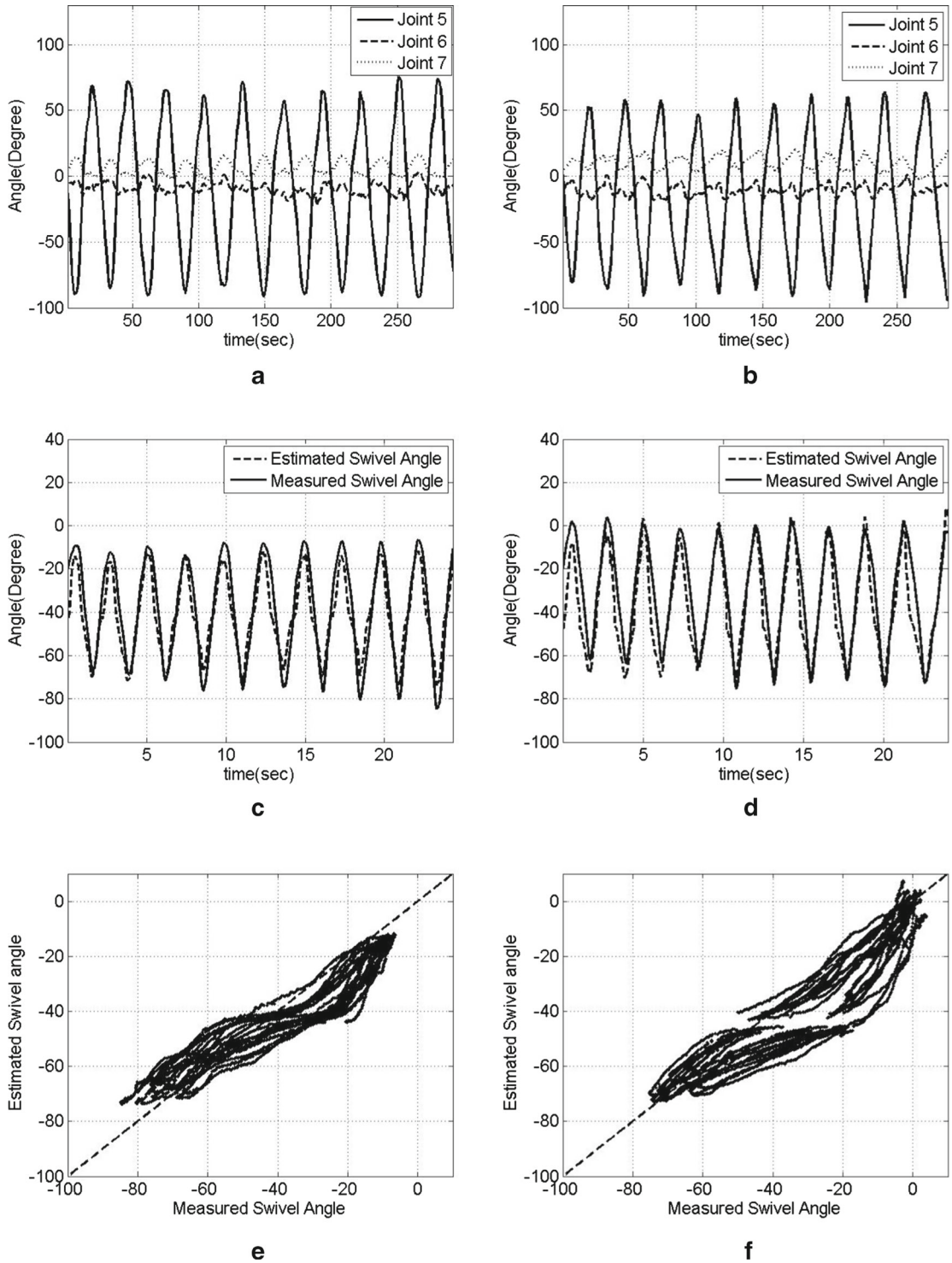

Fig. 11 Swivel angle as a function of wrist orientation. The first ((**a**), (**c**), (**e**)) and second ((**b**), (**d**), (**f**)) column show the comparison result between the estimated and measured swivel angle for subject 1 at P_{m1} and P_{d1} respectively. The first row's data corresponds to $\theta_5(t)$, $\theta_6(t)$ and $\theta_7(t)$ on the wrist which are the input to the swivel angle estimation algorithm. The second row shows the comparison result between the estimated and measured swivel angle at P_{m1} and P_{d1}. The third row plots the estimated swivel angle versus the measured swivel angle

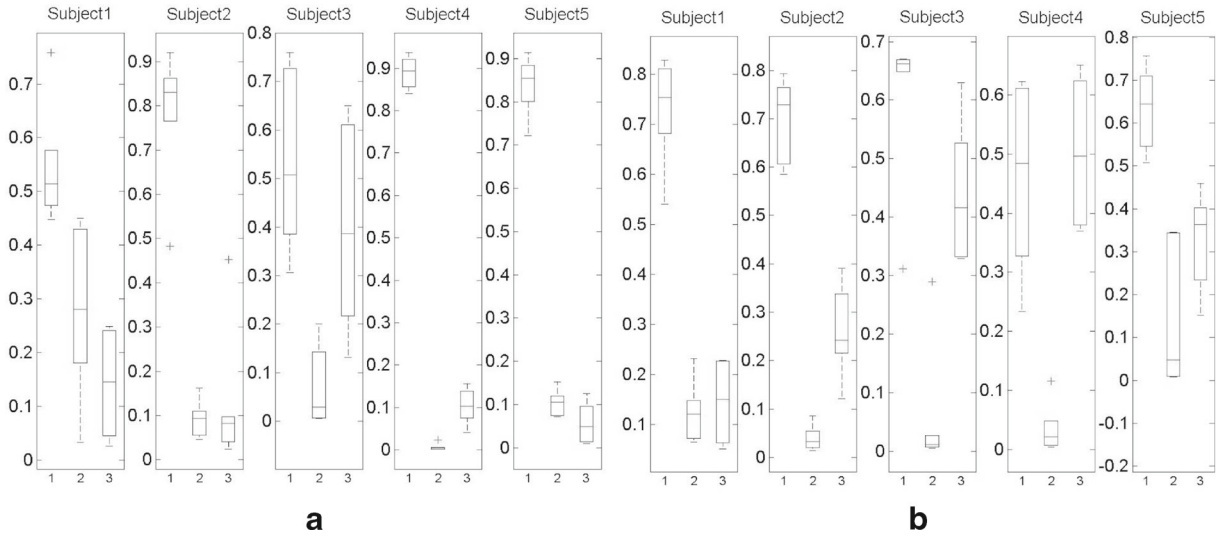

Fig. 12 Statistical analysis of weighting coefficients to define the ergodic function. The mean and variance of the weighting coefficients calculated for 6 different positions in Fig. 9**a** when the rotation around joint five is negative (wrist rotation toward body), **b** when the rotation around joint five is positive

Table 2 Weighting coefficient for wrist joints and regulation coefficient estimated for each subjects

$\phi_{fin} \leq \phi_{ref}$	Subj1	Subj2	Subj3	Subj4	Subj5	Subj6	Subj7	Subj8	Subj9	Subj10
w_1	0.52	0.83	0.51	0.88	0.87	0.91	0.64	0.67	0.77	0.61
w_2	0.32	0.08	0.06	0.01	0.09	0.04	0.14	0.16	0.12	0.13
w_3	0.15	0.08	0.40	0.10	0.03	0.05	0.20	0.15	0.10	0.24
λ	0.11	0.17	0.21	0.12	0.10	0.30	0.14	0.28	0.19	0.09
$\phi_{fin} > \phi_{ref}$	Subj1	Subj2	Subj3	Subj4	Subj5	Subj6	Subj7	Subj8	Subj9	Subj10
w_1	0.76	0.68	0.65	0.48	0.64	0.56	0.67	0.57	0.82	0.75
w_2	0.1	0.04	0.02	0.89	0.87	0.2	0.14	0.06	0.02	0.1
w_3	0.15	0.26	0.37	0.89	0.87	0.23	0.19	0.36	0.14	0.11
λ	0.13	0.12	0.19	0.14	0.31	0.23	0.24	0.11	0.12	0.27

Table 3 Interaction Energy between robot and 10 subjects for Set 1, 2, 3, and 4 in Fig. 10

	Set 1 (J)	Set 2 (J)	Set 3 (J)	Set 4 (J)	Overall (J)
With swivel angle support					
Mean	10.84	13.77	19.01	18.87	15.62
95 % confidence interval	1.10	1.31	1.12	1.16	1.17
Without swivel angle support					
Mean	8.53	12.32	16.34	12.45	12.41
95 % confidence interval	1.12	1.28	1.27	1.02	1.17
% improvement	21.3	10.5	14.04	34	20.6

reach the farthest small balls from the center ball following the straight line. Except for the swivel angle support, the gravity and friction compensations are running as common background controller in the UL-EXO7 [15]. Then each subject repeats the game five times with and without the proposed swivel angle control scheme [Fig. 2] for the comparison of the energy exchange between robot and subjects. For each trial the energy exchange between the two systems can be calculated by integrating the power which can be achieved by multiplying the recorded force/torque sensor data by its respective velocity. The velocities at each sensor are calculated by differentiating the position of each sensor. Table 3 shows the averaged interaction energy for each game set defined in Fig. 10.

5 Conclusions and Discussion

The goal of this study was to propose a closed form redundancy resolution mechanism of the human arm as a viable control scheme for an exoskeleton robot. The criteria for resolving the human arm redundancy was experimentally verified and validated for a wearable robotic application. It is shown in Table 1 that the average absolute error between measured and estimated swivel angle is on average 3.98 and 3.77 degree for ϕ_{ref} and $\Delta\phi$ respectively. The direct comparison result in Figs. 11 and 8 also shows not only the low average error but also the high correlation between the estimated and measured swivel angle. For the swivel angle estimation based on the wrist orientation, the joint availability function was employed and the result in Fig. 12 shows that w_1' has a dominant effect on $\Delta\phi$ while w_3 is the least dominant. Since w_1' is for the rotation around joint five at the wrist, it implies that the muscular coupling between joint five and the swivel angle is stronger than other joint couplings for the given tasks in our experiment. Summarizing all the result so far, we can conclude that most of the unconstrained reaching and grasping tasks with wrist orientation changes can be successfully reproduced based on our redundancy resolution algorithm. In addition Table 3 also reveals that the exoskeleton with swivel angle support can reduce the energy exchange by up to 34 %.

In comparison with our previous work [17], it was shown that the energy exchange could be reduced by 20 % with swivel angle estimation and admittance control in the peg-in-hole test of which the hand trajectory is a combination of Set 1 and Set 4 in Fig. 10. The proposed work in this paper could achieve a similar energy reduction performance which is 21.3 % in Set 1 but it could achieve 34 % energy reduction performance in Set 4 which requires more sophisticated swivel angle changes during the arm movement. Unlike the proposed work in this paper, the swivel angle estimation in our previous work only predicted the reference swivel angle and compensated an excessive swivel angle with a passive admittance control. This can't avoid the physical contact between human and robot to determine the assistive joint torque.

It implies that the transparency of the exoskeleton to the user can be significantly improved by adopting more active swivel angle estimation proposed in this paper to the controller. In a forward kinematic of the robotic manipulator that has the same degree of freedom such as EXO-UL7, the swivel angle is mathematically represented as a function of shoulder joints which is connected to the heavier links and structure than those of other joints. In general, the wearer should overcome the relatively high friction and inertial dynamics without any compensation mechanism. Since the weight of the robotic link on the wrist is lighter than any other arm link, relating the wrist position and orientation to the swivel angle can be exploited as an intuitive and practical control scheme to improve the transparency between wearer and the exoskeleton robot. Figure 13 shows the controlled arm configuration for the given wrist position with the different wrist orientation changes. The inverse kinematics as a function of wrist joint angles provides a stable and closed form solution that does not require iterative operation. Furthermore the proposed algorithm can be easily extended to a higher order control system model such as gradient projection method to achieve a more natural continuous movement. In the gradient projection the choice of the objective function such as manipulability optimization, joint range, obstacle avoidance, torque optimization and etc is critical to the joint angle estimation performance and the proposed swivel angle estimation combined with the joint range limit function can act as the objective function of gradient projection method [19].

The proposed control system can be applied to the exoskeleton robot designed for not only human

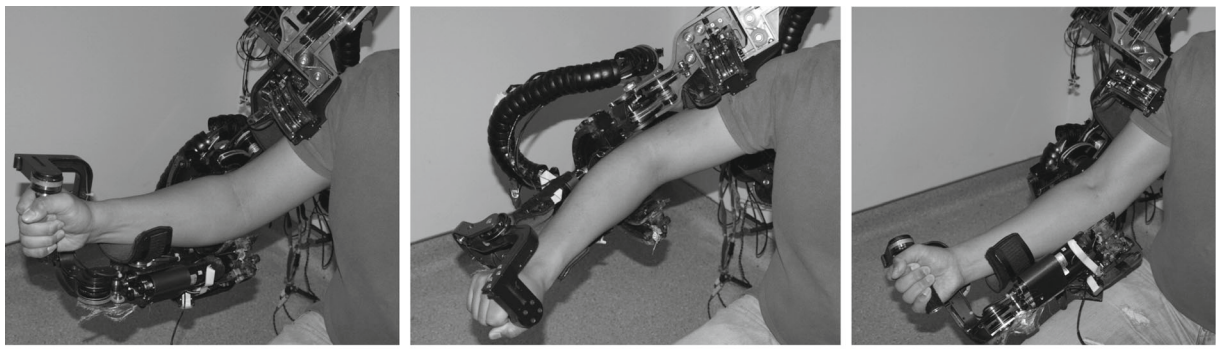

Fig. 13 Swivel angle estimation applied to the EXO-UL7 **a** Swivel angle ϕ_{ref} for the given wrist position without wrist orientation change **b** Swivel angle $\phi_{ref} - \Delta\phi$ for the given wrist position with wrist orientation change **c** $\phi_{ref} + \Delta\phi$ for the given wrist position with wrist orientation change

power augmentation but also rehabilitation programs such as post-stroke rehabilitation. Especially for the emerging bilateral rehabilitation program [15, 16] in which the healthy arm provides assistive force to the impaired arm based on master-slave control, the robot can provide the healthy side of the arm with the proposed synchronization control scheme to significantly extend the rehabilitation session time. Since most of the post-stroke patients have a weak muscle strength even in the healthy arm, it is very challenging for them to move the heavy exoskeleton without proper assistive force for a sufficient amount of time. In some cases, intensive practice during the therapy can put the patient at risk for another injury.

In addition the proposed algorithm computes all the important parameters for the controller off-line and imports the pre-determined parameters to the controller such that it is computationally efficient. Since it is shown in our pilot study that the proposed work could significantly improve the human-robot interaction, more sophisticate and comprehensive experiment needs to be setup to fully understand the human motor control as a future work.

Appendix

Let the plan S be defined by three points P_w, P_e and P_s. The longest axis of the manipulability ellipsoid is aligned along plane S and its magnitude σ_1 is defined as

Lemma 2

$$\begin{aligned}\sigma_1 &= \sqrt{\lambda_1} \\ &= \sqrt{\left(\left(L_{ws}^2 + L_{we}^2\right) + \left(L_{ws}^2 + L_{we}^2\right) c_1\right)/2} \\ c_1 &= \sqrt{1 - c_2}, \\ c_2 &= 4L_{we}^2 L_{ws}^2 \sin(\varphi)^2 / \left(L_{ws}^2 + L_{we}^2\right)^2,\end{aligned} \tag{40}$$

where $L_{ws} = \|P_w - P_s\|$ and $L_{we} = \|P_w - P_e\|$. This result is based on the following derivation and only the right hand side of the human arm is considered for analysis.

Proof A new coordinate frame is defined with an origin at P_s [Fig. 3a] for the computational purpose. In this frame, the z axis is orthogonal to the plane S and the x axis is aligned with the vector $(P_w - P_s)$. Then the relationship between the end-effector velocity $\dot{\mathbf{P}} = [\dot{x_w}\dot{y_w}\dot{z_w}]^T$ and the joint velocity $\dot{\theta}_{1234} = [\dot{\theta_1}\dot{\theta_2}\dot{\theta_3}\dot{\theta_4}]^T$ is defined as follows:

$$\begin{aligned}\dot{\mathbf{P}} &= \mathbf{J}\dot{\theta}_{1234} = [\mathbf{J}_1\ \mathbf{J}_2\ \mathbf{J}_3\ \mathbf{J}_4]\dot{\theta}_{1234}, \\ \mathbf{J}_i &= \begin{cases} \omega_i' \times (P_w - P_s), i = 1, 2, 3 \\ \omega_i' \times (P_w - P_e), i = 4 \end{cases},\end{aligned} \tag{41}$$

where ω_i' denotes the rotation axis of the ith joint. By introducing a new variable φ [Fig. 3a] to represent $\mathbf{J}_4$

and using the fact that $\omega_1' = \mathbf{x}$, $\omega_2' = \mathbf{y}$ and $\omega_3' = \mathbf{z}$ in Fig. 3a, we have

$$\dot{\mathbf{P}} = \begin{pmatrix} 0 & 0 & -L_{we}\sin(\varphi) \\ 0 & L_{ws} & L_{we}\cos(\varphi) \\ -L_{ws} & 0 & 0 \end{pmatrix} \dot{\theta}_{234} = \mathbf{J}_{234}\dot{\theta}_{234} \quad (42)$$

where the full derivation for Eq. 42 can be found in [18]. According to the singular value decomposition, $\mathbf{J}_{234}$ can be represented as $\mathbf{J}_{234} = \mathbf{U}\mathbf{D}\mathbf{V}^T$ where $\mathbf{U} = [u_1\ u_2\ u_3]$, $\mathbf{V} = [v_1\ v_2\ v_3]$ and $\mathbf{D} = diag[\sigma_1\ \sigma_2\ \sigma_3]$. The u_i in the left singular vector $\mathbf{U}$ indicates one of the three axis constructing the manipulability ellipsoid and singular value σ_i in $\mathbf{D}$ indicates the magnitude of u_i as shown in Fig. 3b. Note that u_i and σ_i are the eigenvectors and square root of the non-zero eigenvalues of $\mathbf{J}_{234} \cdot \mathbf{J}_{234}^*$. Solving $\det\left(\mathbf{J}_{234} \cdot \mathbf{J}_{234}^* - \lambda\mathbf{I}\right) = 0$ allows to obtain u_i and $\sigma_i\ \left(= \sqrt{\lambda_i}\right)$. Based on Sarrus's rule [22] the following expressions for the eigenvalues are obtained:

$$\begin{aligned} \lambda_{1,2} &= \frac{\left(L_{ws}^2 + L_{we}^2\right) \pm \left(L_{ws}^2 + L_{we}^2\right) c_1}{2}, \\ \lambda_3 &= L_{ws}^2\ (\lambda_1 > \lambda_2),\ c_1 = \sqrt{1 - c_2}, \\ c_2 &= 4L_{we}^2 L_{ws}^2 \sin(\varphi)^2 / \left(L_{ws}^2 + L_{we}^2\right)^2. \end{aligned}$$

One may note that $0 \le c_2 \le 1$ and $0 \le c_1 \le 1$ such that $\lambda_{1,2}$ are non complex numbers. The relationships between λ_1, λ_2 and λ_3, is studied by using two individual cases: □

Case 1 $(L_{ws} \ge L_{we})$

$$\begin{aligned} \lambda_1 - \lambda_3 &= \frac{\left(L_{ws}^2 + L_{we}^2\right) + \left(L_{ws}^2 + L_{we}^2\right) c_1}{2} - L_{ws}^2 \\ &\ge \frac{\left(L_{we}^2 - L_{ws}^2\right) + \left(L_{ws}^2 + L_{we}^2\right) c_{min1}}{2} \\ &= \frac{\left(L_{we}^2 - L_{ws}^2\right) + \left(L_{ws}^2 + L_{we}^2\right) \sqrt{1 - c_{max2}}}{2} \\ &= \frac{\left(L_{we}^2 - L_{ws}^2\right) + \sqrt{\left(L_{ws}^2 - L_{we}^2\right)^2}}{2} = 0, \end{aligned} \quad (43)$$

where c_{min1} and c_{max2} are the minimum and maximum values of c_1 and c_2 respectively. The term c_{max2} in Eq. 49 is defined as:

$$\begin{aligned} c_{max2} &= \max\left(4L_{we}^2 L_{ws}^2 \sin(\varphi)^2\right) / \left(L_{ws}^2 + L_{we}^2\right)^2 \\ &= 4L_{we}^2 L_{ws}^2 / \left(L_{ws}^2 + L_{we}^2\right)^2. \end{aligned}$$

Case 2 $(L_{ws} < L_{we})$

$$\begin{aligned} \lambda_1 - \lambda_3 &= \frac{\left(L_{ws}^2 + L_{we}^2\right) + \left(L_{ws}^2 + L_{we}^2\right) c_1}{2} - L_{ws}^2 \\ &\ge \frac{(1 + c_{min1})\left(L_{ws}^2 + L_{we}^2\right)}{2} - L_{ws}^2 \\ &= \frac{\left(L_{we}^2 - L_{ws}^2\right)}{2} \ge 0, \end{aligned} \quad (44)$$

where the first inequality in Eq. 44 is based on the fact that $c_{min1} = \min[c_1] = 0$. The second inequality in Eq. 44 is valid since $L_{ws} < L_{we}$. Therefore we conclude that $\lambda_1 \ge \lambda_3$ for all possible values of L_{ws}. It implies that the magnitude of the longest axis in the manipulability ellipsoid is

$$\sigma_1 = \sqrt{\lambda_1} = \sqrt{\left(\left(L_{ws}^2 + L_{we}^2\right) + \left(L_{ws}^2 + L_{we}^2\right) c_1\right)/2}. \quad (45)$$

Based on the fact that the direction of the major axis of the manipulability ellipsoid corresponds to the eigenvector of the following (46), the eigenvector u_1 is obtained by applying the corresponding eigenvalue λ_1 to λ in Eq. 46:

$$\left(\mathbf{J}_{234} \cdot \mathbf{J}_{234}^*\right)\mathbf{X} = \lambda\mathbf{X}, \quad \mathbf{X} = [x\ y\ z]^T. \quad (46)$$

Then the direction of the eigenvector $\mathbf{X}$ in Eq. 46 is defined as:

$$y = \frac{L_{we}^2 \sin(\varphi)^2 - \lambda_1}{L_{we}^2 \sin(\varphi)\cos(\varphi)} x,\ z = 0. \quad (47)$$

Considering the joint limit of the exoskeleton robot [37], it is assumed that $0 < \varphi \le \pi/2$. Note that when $\varphi = 0$, the arm is in a singular position. Then the numerator in Eq. 47 can be rewritten as:

$$\begin{aligned} &\lambda_1 - L_{we}^2 \sin(\varphi)^2 \quad (48) \\ &= \frac{\left(L_{ws}^2 + L_{we}^2\right)(1 + c_1)}{2} - L_{we}^2 \sin(\varphi)^2 \\ &= \frac{\left(L_{ws}^2 + L_{we}^2\right)\left(1 + \sqrt{1 - \frac{4L_{we}^2 L_{ws}^2 \sin(\varphi)^2}{\left(L_{ws}^2 + L_{we}^2\right)^2}}\right)}{2} - L_{we}^2 \sin(\varphi)^2 \\ &\ge \frac{\left(L_{ws}^2 + L_{we}^2\right) + \left|L_{ws}^2 - L_{we}^2\right| - 2L_{we}^2 \sin(\varphi)^2}{2} \\ &= \frac{\left(L_{ws}^2 - L_{we}^2\right) + \left|L_{ws}^2 - L_{we}^2\right| + 2L_{we}^2 \cos(\varphi)^2}{2} \\ &= \frac{2L_{we}^2 \cos(\varphi)^2}{2} \ge L_{we}^2 \cos(\varphi)^2 \ge 0. \quad (49) \end{aligned}$$

By plugging Eq. 48 into Eq. 47, we can conclude that the slope in Eq. 47 becomes negative. Figure 3c depicts the direction of u_1 on plane S.

References

1. Asfour, T., Dillmann, R.: Human-like motion of a humanoid robot arm based on a closed-form solution of the inverse kinematics problem. In: Proceeding of IEEE/RSJ International Conference On Intelligent Robots and Systems, vol. 2, pp. 27–31 (2003)
2. Badler, N.I., Tolani, D.: Real-time inverse kinematics of the human arm. Presence **5**(4), 393–401 (1996)
3. Cavallaro, E.E., Rosen, J., Perry, J.C., Burns, S.: Real-time myoprocessors for a neural controlled powered exoskeleton arm. IEEE Trans Biomed Eng **21**, 2387–2396 (2006)
4. Chen, I.M., Gao, Y.: Closed-form inverse kinematics solver for reconfigurable robots. In: Proceedings of the IEEE International Conference on Robotics and Automation, vol. 3, pp. 2395–2400. Seoul, Korea (2001)
5. Dum, R., Strick, P.: Motor Areas in the frontal Lobe: The Anatomical Substrate for the Central Control of Movement. In: Motor Cortex in Voluntary Movements. CRC press (2005)
6. Gielen, C., Vrijenhoek, E.J., Flash, T.: Neggers., S.: Arm position constraints during pointing and reaching in 3-d space. J. Neurophys. **78**(2), 660–673 (1997)
7. Gielen, C., Vrijenhoek, E.J., Flash, T., Neggers, S.: Review of models for the generation of multi-joint movements in 3-d. Advances in experimental medicine and biology. Prog. Mot. Control. **629**, 523–550 (2009)
8. Graziano, M.S., Taylor, C.S., Moore, T.: Complex movements evoked by micro stimulation of precentral cortex. Neuron **30**(30;34(5)), 841–851 (2002)
9. Green, P.J., Silverman, B.W.: Nonparametric regression and generalized linear models. Number 58 in Monographs on Statistics and Applied Probability. Chapman and Hall (1994)
10. Haykin, S. Adaptive Filter Theory, Fourth edition. MA, Prentice Hall, Reading (2002)
11. Hill, A.V.: The heat of shortening and the dynamic constants of muscle. In: Proceedings R. Soc. London Ser B, vol. 126, pp. 136–195 (1938)
12. Kang, T., He, J., Tillery, S.I.H.: Determining natural arm configuration along a reaching trajectory. Exp Brain Res **167**(3), 352–361 (2005)
13. Kim, H.: systematic control and application for 7 dof upper-limb exoskeleton. University of California Santa Cruz, Ph.D. thesis (2012)
14. Kim, H., Li, Z., Milutinovic, D., Rosen, J.: Resolving the redundancy of a seven dof wearable robotic system based on kinematic and dynamic constraint. In: The Proceedings of 2012 IEEE International Conference on Robotics and Automation. Saint Paul, Minnesota, USA (2012)
15. Kim, H., Miller, L.M., Fedulow, I., Simkins, M., Gabriel, A., Nancy, B., Rosen, J.: Kinematic data analysis for post-stroke patients following bilateral versus unilateral rehabilitation with an upper limb wearable robotic system. IEEE Trans Neural Syst Rehabil Eng **21**, 153–164 (2013)
16. Kim, H., Miller, L.M., Li, Z., Roldan, J.R., Rosen, J.: Admittance control of an upper limb exoskeleton–reduction of energy exchange. In: Proceedings of the IEEE EMBC. San Diego, USA (2012)
17. Kim, H., Miller, L.M., Nancy, B., Gabriel, A., Rosen, J.: Redundancy resolution of the human arm and an upper limb exoskeleton. IEEE Trans. Biomed. Eng. **59**, 1770–1779 (2012)
18. Kim, H., Miller, L.M., Rosen, J.: Redundancy resolution of a human arm for controlling a seven dof wearable robotic system. In: Proceedings of the IEEE EMBC. Boston, USA (2011)
19. Kim, H., Roldan, J.R., Li, Z., Rosen, J.: Viscoelastic model for redundancy resolution of the human arm via the swivel angle: Applications for upper limb exoskeleton control. In: Proceedings of the IEEE EMBC. San Diego, USA (2012)
20. Krebs, H.I., Hogan, N., Aisen, M.L., Volpe, B.T.: Robot-aided neurorehabilitation. Rehabilitation Engineering. IEEE Transactions on [see also IEEE Transactions on Neural Systems and Rehabilitation] pp. 75–87 (1998)
21. Kriesel, D.: A Brief Introduction to Neural Networks. (2007). http://www.dkriesel.com
22. Lay, D.C.: Linear Algebra and Its Applications, Third edition. Addison Wesley (2005)
23. Lee, P., Wei, S., Zhao, J., Badler, N.I.: Strength guided motion. Comput. Graph. **24**(4), 253–262 (1990)
24. Liang, T.C., Liu*, J.S.: An improved trajectory planner for redundant manipulators in constrained workspace. J. Robot. Syst. **16**(6), 339–351 (1999)
25. Liegeois, A.: Supervisory control of the configuration and behavior of multibody mechanisms. IEEE Trans. Syst. Man., Cybernetics SMC-7, pp. 868–871 (1977)
26. Maciejewski, A.A.: Dealing wit the ill-conditioned equations of motion for articulated figures. IEEE Computer Graphics and Applications pp. 63–71 (1990)
27. Marjan, A., Martijn, J.K., Stan, C.G.: Modeling kinematics and dynamics of human arm movements. Mot. Control. **8**(3), 312–338 (2004)
28. Martinez, F., Retolaza, I., Pujana-Arrese, A., Cenitagoya, A., Basurko, J., Landaluze, J.: Design of a five actuated dof upper limb exoskeleton oriented to workplace help. In: Biomedical Robotics and Biomechatronics, vol. 2, pp. 169–174. Tokyo, Japan (2008)
29. Miller, L.M., Kim, H., Rosen, J.: Redundancy and joint limits of a seven degree of freedom upper limb exoskeleton. In: Proceedings of the IEEE EMBC. Boston, USA (2011)
30. Miller, L.M., Rosen, J.: Comparison of multi-sensor admittance control in joint space and task space for a seven degree of freedom upper limb exoskeleton. In: Proceedings of the IEEE RAS and EMBS International Conference on Biomedical Robotics and Biomechatronics(BioRob), pp. 70–75 (2010)

31. Murray, R.M., Li, Z., Sastry, S.S.: A Mathematical Introduction to Robotic Manipulation. CRC Press (1994)
32. Nakamura, Y., Hanafusa, H., Yoshikawa, T.: Taskpriority: Task priority based redundancy control of robot manipulators. Int. J. Robotics pp. 3–15 (1987)
33. Nef, T., Guidali, M., Klamroth-Marganska, V., Riender, R.: Armin-exoskeleton robot for stroke rehabilitation. In: World Congress on Medical Physics and Biomedical Engineering IFMBE, vol. 25/9. Munich, Germany (2009)
34. Panagiotis, K.A., Pantelis, T.K., Kostas, J.K.: A biomimetic approach to inverse kinematics for a redundant robot arm. Auton. Robot. **29**(3-4), 293–308 (2010)
35. Perry, J.C., Rosen, J.: Design of a 7 degree-of-freedom upper-limb powered exoskeleton. In: IEEE/RAS-EMBS International Conference on Biomedical Robotics and Biomechatronics. Pisa, Italy (2006)
36. Perry, J.C., Rosen, J., Burns, S.: Upper-limb powered exoskeleton design. Mechatronics **12**(4), 408–417 (2007)
37. Rosen, J., Perry, J.C.: Upper limb powered exoskeleton. Int. J. Humanoid Robot. **4**(3), 529–548 (2007)
38. Soechting, J., Buneo, C., Herrmann, U., Flanders, M.: Moving effortlessly in three dimensions: Does donders' law apply to arm movement. J. NeuroSci. **15**, 6271–6280 (1995)
39. de Souza Ramos, J.L.A., Meggiolaro, M.A.: Use of surface electromyography to control an active upper limb exoskeleton actuated by pneumatic artificial muscles and optimized with genetic algorithms. In: 22nd International Congress of Mechanical Engineering. Ribeirao Preto, Brazil (2013)
40. Tolani, D., Goswami, A., Badler, N.I.: Real-time inverse kinematics techniques for anthropomorphic limbs. Graph. Model. Image Process. **62**(5), 353–388 (2000)
41. Uno, Y., Kawato, M., Suzuki, R.: Formation and control of optimal trajectory in human multi joint arm movement. Biol. Cybern. **61**(2), 89–101 (1989)
42. Yan, G.: Decomposible closed form inverse kinematics for reconfigurable robots using product-of-exponentials formula. Master's thesis, Nanyang Technological University (2000)
43. Ying, L., Xu, D., Liang, Z.P.: On tikhonov regularization for image reconstruction in parallel mri. In: Proceedings of the 26th Annual International Conference of the IEEE EMBS. San Francisco, USA (2004)
44. Zoss, A., Kazerooni, H., Chu, A.: On the mechanical design of the berkeley lower extremity exoskeleton (bleex). In: IEEE/RSJ International Conference on Intelligent Robots and Systems. Alberta, Canada (2005)